GEOPHYSICS, VOL. 71, NO. 6 (NOVEMBER-DECEMBER 2006); P. F147–F159, 14 FIGS., 2 TABLES.
10.1190/1.2345053

Low-frequency seismic properties of thermally cracked and argon-saturated granite

Cao Lu[1] and Ian Jackson[2]

ABSTRACT

Torsional forced-oscillation techniques have been used to measure the shear modulus and strain-energy dissipation on cylindrical specimens of a fine-grained granite, Delegate aplite. The specimens were subjected to thermal cycling and associated microcracking under varying conditions of confining pressure P_c and argon pore-fluid pressure P_f within the low-frequency saturated isobaric regime. Complementary transient-flow studies of in-situ permeability and volumetric measurements of connected crack porosity allowed the modulus measurements to be interpreted in terms of the density and interconnectivity of the thermally generated cracks. The modulus measurements indicate that newly generated thermal cracks are closed by a differential pressure, $P_c - P_f$, which ranges from $\sim$120 to 160 MPa for temperatures of 300–600°C. This suggests crack aspect ratios on the order of 10^{-3}. The covariation of in-situ permeability k and thermal crack density ε that we infer from the modulus deficit is consistent with percolation theory. There is a well-defined threshold at $\varepsilon_c \sim 0.17$, beyond which k increases markedly as $(\varepsilon - \varepsilon_c)^{\nu}$, with $\nu \sim 2$. At lower crack densities, it is difficult to measure the sensitivity of shear modulus to variations of confining and pore pressures because pore-pressure equilibrium is approached so sluggishly. At temperatures beyond the percolation threshold, the modulus variation is a function of the effective pressure, $P_{\text{eff}} = P_c - nP_f$, with the value of n increasing toward one with increasing crack connectivity.

INTRODUCTION

Over the past few decades, researchers have become increasingly aware of the need to account for the frequency dependence (dispersion) of elastic wave speeds and the associated attenuation in fluid-saturated rocks in seismic interpretation (e.g., Gordon, 1974; Mavko and Nur, 1975; O'Connell and Budiansky, 1977; Murphy, 1984; Winkler, 1985; Paffenholz and Burkhardt, 1989; Jackson, 1991; Mavko and Jizba, 1991; Dvorkin and Nur, 1993; Le Ravalec and Guéguen, 1996; Schubnel and Guéguen, 2003). The immense frequency interval separating the megahertz frequencies of the ultrasonic methods employed in most laboratory studies from the subkilohertz frequencies used in geophysical exploration of the upper crust presents a particular challenge. Saturation with a relatively incompressible bulk pore fluid capable of stress-induced flow within the pore space should result in generally higher and frequency-dependent effective moduli. There is also strong experimental evidence to suggest that low concentrations of adsorbed volatiles may reduce the elastic moduli of rocks by influencing the energetics of and cohesive forces between silicate (especially quartz) mineral surfaces in intimate contact (King, 1966; Tittmann et al., 1980; Spencer, 1981; Murphy et al., 1984).

The theoretical description of rocks as porous/cracked media often involves the calculation of effective elastic moduli for a composite derived by embedding pores or cracks of prescribed geometry into a medium that initially has zero porosity (e.g., Walsh, 1969; O'Connell and Budiansky, 1974; Hudson, 1981; Kachanov, 1993; Pointer et al., 2000; Chapman et al., 2002). An alternative, essentially phenomenological approach to obtaining the elastic moduli for fluid-saturated rocks relates the effective moduli for the fluid-saturated medium to those of the same medium under dry conditions, thus avoiding the need to specify the geometry of the pore space (e.g., Gassmann, 1951; Biot, 1956a, b; Gardner, 1962; Mavko and Jizba, 1991).

Both approaches have been used, especially for porous sedimentary rocks and sometimes in conjunction with experimental data, to estimate the substantial amount of dispersion to be expected for fluid flow on various spatial scales (e.g., Winkler, 1985, 1986; Mavko and Jizba, 1991; Le Ravalec and Guéguen, 1996). However, there have so far been very few direct experimental observations of the expected modulus relaxation in fluid-saturated rocks of relatively low porosity (Gordon, 1974; Spencer, 1981; Tittmann et al., 1984; Murphy, 1985; Paffenholz and Burkhardt, 1989), and it is difficult to evaluate

Manuscript received by the Editor August 8, 2005; revised manuscript received February 27, 2006; published online October 13, 2006.
[1]Deceased December 18, 1996.
[2]Australian National University, Research School of Earth Sciences, Canberra ACT, Australia 0200. E-mail: ian.jackson@anu.edu.au.

the observed dispersion and attenuation in terms of fluid flow. To address these problems, we investigated the low-frequency shear-mode behavior of thermally cracked and fluid-saturated rock by conducting torsional forced-oscillation experiments at subhertz frequencies.

EXPERIMENTAL PROCEDURE

Granite specimen and argon pore fluid

For this study, we have chosen an aplite from Delegate, New South Wales, Australia. It was previously described by Lu and Jackson (1998), who showed that stable, thermally supported populations of microcracks could be generated in this rock. Delegate aplite is a granitic rock of 0.5 mm average grain size, with a bulk density of 2.57 g/cm^3 and a total porosity of 2.3%, of which about one third is accessible to water saturation. Heating in air to 800°C results in a weight loss of 0.25%.

The use of argon as a chemically inert pore fluid permits us to evaluate the purely hydraulic effects of fluid saturation without the complication of the chemical effects of adsorbed molecules and polar fluids. Under the conditions of pore pressure P_f and temperature T used in this study, argon is a single-phase fluid. Its key physical properties are its density ρ, isothermal bulk modulus K_f or incompressibility, and viscosity η. Figure 1 shows a graph of these properties plotted against pressure. Argon's density varies from about 10% to 110% of the density of water at standard conditions, whereas K_f and η are each lower than the corresponding quantities for water by about an order of magnitude.

Forced-oscillation measurements of shear modulus and strain-energy dissipation

Jackson and Paterson (1987, 1993) described a torsional forced-oscillation technique for the study of rock viscoelasticity at teleseismic frequencies (mHz-Hz), high temperature, and moderate confining pressure. An elastic standard of known elastic modulus and negligible internal friction is connected mechanically in series with a compound assembly comprising a cylindrical rock specimen mounted between alumina torsion rods, all jacketed within a thin-walled steel sleeve. Thus, the entire assembly is exposed to the same applied torque. At sufficiently low frequencies, the phase of the sinusoidally time-varying torque is essentially uniform throughout the assembly. By measuring the relative amplitudes and phase of the torsional distortions of the elastic standard and the specimen assembly, the shear modulus G and the associated strain energy dissipation Q^{-1} at maximum strain amplitudes of about 10^{-5} can be determined. The procedures for analyzing the forced-oscillation data are described by Lu and Jackson (1998).

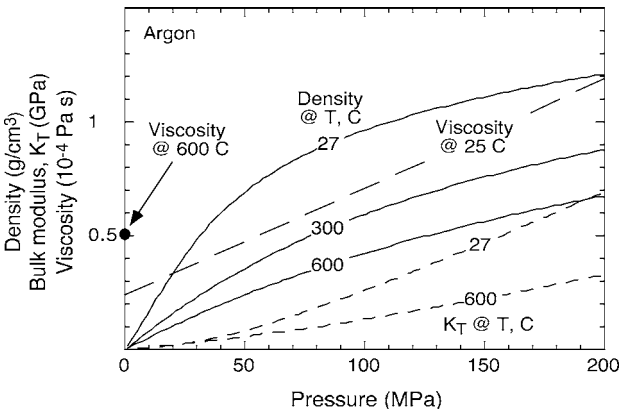

Figure 1. Key thermophysical properties of argon as a pore fluid. The density ρ and isothermal bulk modulus, $K_T = \rho v^2/[1 + T(\alpha v)^2/C_p]$, are derived from Stewart and Jacobsen (1989), where α is the thermal expansivity, v is the sound speed, and C_p is the specific heat at constant pressure. The viscosity η is from Kaye and Laby (1973) and Vidal et al. (1979). The corresponding properties of water at ambient conditions are $\rho = 1.0$ g cm^{-3}, $K_T = 2.0$ GPa, and $\eta = 9 \times 10^{-4}$ Pa-s (e.g., Kaye and Laby, 1973).

Configuration of pore-fluid system

The argon pore/fluid system which was newly implemented for this study consists of upstream and downstream reservoirs connected to the respective ends of the specimen assembly (Figure 2). O-ring seals at the upper and lower ends of the steel jacket isolate the pressurized interior of the pressure vessel from the upstream and the downstream pore-fluid reservoirs. The upstream reservoir is composed of a volumeter driven by a dc motor, an air-operated valve, a connecting pipe, and a hardened steel piston. The downstream reservoir includes the space within the hollow lower (steel) part of the compound experimental assembly, the lower vent tube, and an air-operated valve. A filter has been placed at the entrance to the lower vent tube to reduce the likelihood of blockage from possible contamination from inside the pore-fluid system.

The fluid pressures in the upstream and the downstream reservoirs are measured with two high-pressure transducers (Precise Sensors, model 114) that have a resolution of 0.1 mV/10 V (equivalent to

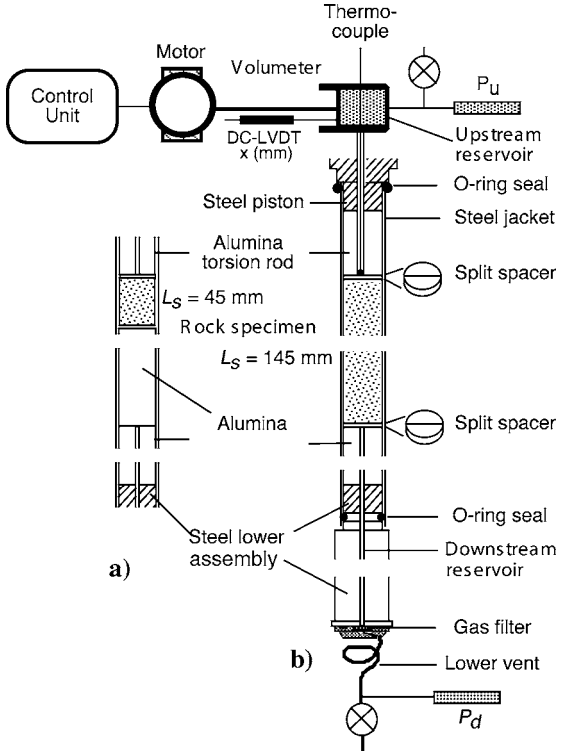

Figure 2. Experimental configuration for (a) measurements of crack porosity; and (b) measurements of shear modulus, attenuation and permeability.

about 0.05/500 MPa), calibrated against a Bourdon-tube (Heise) pressure gauge. The piston position within the volumeter was monitored by a suitably calibrated dc LVDT (model 500HR-DC, Schaevitz Engineering). Digital data was acquired by a multichannel digital acquisition card through a 5B Series backplane signal conditioner (Analog Devices Inc.) with LabVIEW software support (National Instruments). Both pore pressures and the displacement of the upstream volumeter piston were digitally recorded as functions of time.

For the purpose of studying the permeability of the rock specimen, it is vital that pore fluid should flow only through the rock. Therefore, a good seal is needed in the specimen assembly to prevent any short-circuit flow path between the steel jacket and the rock. In practice, it was found that a prior excursion to temperatures near 600°C at confining pressure $P_c > 50$ MPa was sufficient to establish satisfactory contact between the cylindrical surface of the rock specimen and the enclosing steel jacket.

Measurement of connected porosity

The pressure sensitivity of fluid storage within any reservoir (including the pore space of a rock specimen) is given by its storage capacity S, defined as

$$S = (1/\rho_f)(\partial m_f/\partial P) \sim V_f/K_f, \quad (1)$$

where m_f is the mass of fluid, with density ρ_f and bulk modulus K_f, stored within the reservoir of volume V_f under the prevailing conditions of pressure P and temperature T. The approximation in equation 1 reflects the fact that the bulk moduli for a porous rock and for its crystalline matrix are typically each on the order of $100 \times K_f$ (e.g., Zhang et al., 1994). For a rock specimen of total volume V_s and connected porosity ϕ_c, the specific storage capacity (or storativity) is thus

$$B_s = S/V_s \sim \phi_c/K_f. \quad (2)$$

Zhang et al. (1994) described a pore-pressure-incrementing technique for the in-situ measurement of connected crack porosity. With the downstream reservoir disconnected (Figure 2), one first establishes a state of uniform fluid pressure P_u in the upstream reservoir and rock specimen. The piston in the upstream volumeter is then advanced to generate a small pressure increment in the upstream reservoir. The temporal covariation of P_u and the position x of the volumeter piston is monitored as fluid penetrates the pore space of the specimen, eventually establishing a new state of uniform fluid pressure throughout. Zhang et al. (1994) showed that, by assuming conservation of fluid mass and using the approximation to specimen storativity given by equation 2, the porosity is given as follows:

$$\phi_c = (A_v K_f/V_s)(\rho_{RT}/\rho_T)[(\Delta x/\Delta P_u)_R - (\Delta x/\Delta P_u)_0], \quad (3)$$

where ρ_{RT} and ρ_T are the densities of pore fluid under pressure P_u, at room temperature (within the volumeter) and at the elevated temperature T (within the rock pore space), respectively; A_v is the cross-sectional area of the volumeter piston, and ΔP_u is the change in pore pressure corresponding to a small displacement Δx of the volumeter piston from the reference position. The first term in the brackets, $(\Delta x/\Delta P_u)_R$, is determined from the measurements taken with the rock specimen (indicated by subscript R); the second term, $(\Delta x/\Delta P_u)_0$, is determined by measuring at the same volumeter piston position x but with a known impermeable standard (subscript 0) as a control. The standard is a specimen of Cape Sorell quartzite, which was shown by Lu and Jackson (1998, their Figure 9) to be essentially impermeable even under the most favorable conditions for fluid flow, that is, at $P_c = 50$ MPa, $T = 600$°C. This latter measurement is essentially a determination of the storage capacity S_u of the upstream reservoir, which is needed for the analysis of the permeability measurements; S_u is given by

$$S_u = A_v(\Delta x/\Delta P_u)_0. \quad (4)$$

The quantities $(\Delta x/\Delta P_u)_0$ and S_u, are each approximately inversely proportional to K_f (equations 1 and 4) and thus vary significantly with both pressure and temperature (Figure 1).

The quantities $\Delta x/\Delta P_u$ were estimated at $x = 0$ (that is, the position of zero output voltage for the DC-LVDT) by differentiation of least-squares fits to the (x, P_u) data (e.g., Figure 3) for a control specimen of impermeable quartzite (U in Figure 3) and for the samples of Delegate aplite (shortened from 145 to 45 mm length; S in Figure 3) tested under conditions of high permeability ($T \geq 500$°C). Under these circumstances, the volumeter piston could be advanced at controlled speed to cause the required covariation of x and P_u within a few minutes. We determined whether equilibrium had been attained during the dynamic test by measuring x and P_u again, under static conditions at least five minutes after completion of the dynamic test (Figure 3). At lower temperatures and permeabilities, much longer delays (up to hours) were required for pore pressure equilibration so that $(\Delta x/\Delta P_u)_R$ was best approximated by the average ratio of finite differences for positive and negative perturbations from the volumeter piston reference position ($x = 0$). Each determination of connected crack porosity was based on at least four redundant measurements of $(\mathrm{d}x/dP_u)_R$ or $(\Delta x/\Delta P_u)_R$.

The use of equation 3 to determine the connected porosity depends critically on the ability to resolve the difference between the slopes $\mathrm{d}x/\mathrm{d}P_u$ for the two systems, i.e., that containing the granite specimen and that with the control specimen. Most of the error arising from the use of equation 3 is derived from the measurement of $(\mathrm{d}x/\mathrm{d}P_u)_R$.

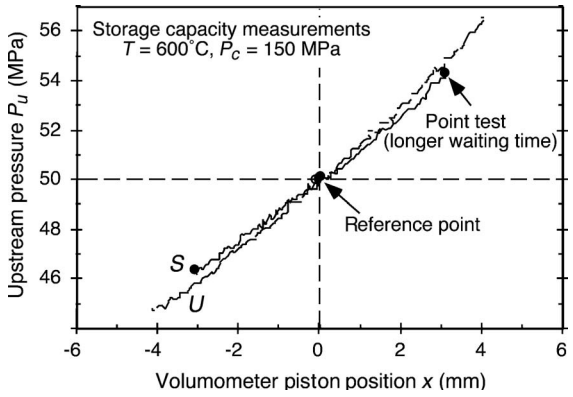

Figure 3. Representative measurements of storage capacity of the upstream reservoir under contrasting conditions: S when connected to a thermally cracked rock specimen and U when connected to a control specimen of impermeable quartzite. The filled circles represent the results of the static tests and their location at the extremities of the continuous record from the dynamic test confirms the maintenance of pore-pressure equilibrium during the latter experiment.

Measurement of permeability by the transient flow method

For relatively large rock specimens of low permeability, long periods of time are required to establish steady flow. So, experimental methods that rely upon the proportionality between the global pressure gradient and the fluid flux (Darcy's law) are impractical. An attractive alternative is the transient-flow method, pioneered by W. F. Brace, in which an equilibrium state of uniform fluid pressure p_0 throughout the system is perturbed by imposition of a small pressure increment Δp in the upstream reservoir (achieved by advancing the volumeter piston). The subsequent decay (or growth) of fluid pressure in the upstream reservoir is monitored (Figure 4).

The fluid flow through the rock specimen is governed by a diffusion equation that must be solved subject to the appropriate initial and boundary conditions. In principle, it is possible to determine both permeability k and storativity B_s by analyzing the pressure-time record from a transient-flow test (Neuzil et al., 1981). However, the storage capacities of the specimens tested in this study are always sufficiently small relative to those of the upstream and downstream reservoirs (S_u and S_d, respectively) for the solution to closely approximate that given by Hsieh et al. (1981) for negligible storativity (Lu, 1996). Under these circumstances, the evolution of the hydraulic head in the upstream reservoir is given by

$$[p(0,t) - p_0]/\Delta p = [S_u + S_d \exp(-At)]/(S_u + S_d), \quad (5)$$

where the rate constant A is expressed as

$$A = (kA_s/\eta L_s S_u)(1 + S_u/S_d) \quad (6)$$

(Brace et al., 1968), where A_s is the cross-sectional area and L_s is the length of the rock specimen. The permeability k is therefore determinable from the experimentally determined exponent A, but the (small) specimen storativity B_s remains unconstrained by the transient flow measurement. For the calculation of k from equation 6, S_u was independently measured as described above, the (pressure-dependent) viscosity η of argon was taken from Vidal et al. (1979), and $S_d \sim V_d/K_f$ was estimated from the geometry of the downstream reservoir and the equation of state of argon (Stewart and Jacobsen, 1989; their Figure 1).

The analysis leading to equations 5 and 6 neglects any variation of fluid properties, notably bulk modulus, across the pressure interval Δp and thus is directly applicable only to measurements conducted above a threshold value of p_0, such that $\Delta p/p_0 \ll 1$. This condition is met in the present study for the measurements with $p_0 > 25$ MPa but not for those of Lu and Jackson (1998) in which the fluid pressure in the upstream reservoir was incremented (Δp of 5–10 MPa) from p_0 = 0.1 MPa. Accordingly, although a rate constant A for exponential decay was inferred from each of these earlier measurements, the robust estimation of k via equation 6 was not possible.

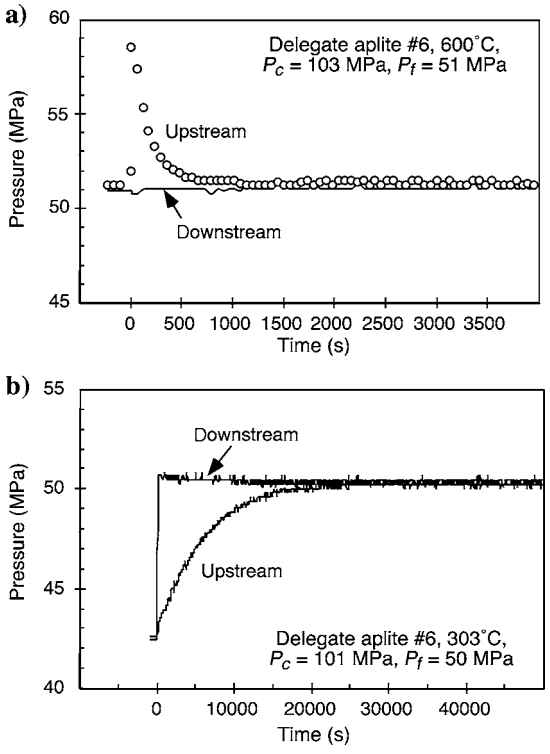

Figure 4. Representative examples of the evolution of the pressure in the upstream reservoir following application of small pressure increments. The exponential decay or growth of P_u is used to measure permeability (see text for details). (a) Delegate aplite specimen #6 at P_c = 103 MPa, unperturbed P_f = 51 MPa, and T = 600°C. The slight change in the downstream pore pressure in response to δP_u is beyond the resolution of these measurements. (b) Delegate aplite specimen #6 at P_c = 101 MPa, P_f = 50 MPa, and T = 303°C. The pore-fluid pressure increment is applied to the downstream reservoir. Pore pressure equilibration occurs much more slowly at the lower temperature.

Adjustment of pore pressure

The downstream reservoir has a much larger volume than the upstream reservoir ($S_d/S_u \sim V_d/V_u \sim 35$). To increase the pore pressure, pressurized argon gas was introduced through an air-operated valve, usually into the downstream reservoir, and allowed to permeate the rock specimen — eventually raising the pressure in the upstream reservoir to the equilibrium value. The time required to reach equilibrium pore pressure is a sensitive function of the permeability of the rock specimen (equation 6). To decrease the pore pressure, argon gas was released from the downstream reservoir through the downstream valve until the prescribed value of pore pressure was reached. The torsional forced-oscillation experiments at prescribed values of differential pressure ($P_{\text{diff}} = P_c - P_f$) and temperature were conducted when the equilibrium state in pore pressure and temperature had been reestablished.

However, for the first series of experiments conducted on Delegate aplite specimen #5 under conditions of low permeability and room temperature, the following alternative procedure was used in adjusting the pore pressure. To reduce the time required for pore-pressure equilibration, confining pressure P_c was initially set to a low value (50 MPa) to maximize the permeability. This allowed the pore pressure to equilibrate at 45 MPa. The confining pressure was then raised to progressively higher values at fixed nominal P_f (see later discussion); higher pore pressures were subsequently achieved through the introduction of additional pore fluid, again initially under conditions of low differential pressure.

RESULTS

Shear modulus

Measurements of shear modulus and internal friction were made on thermally cycled Delegate aplite under conditions of varying confining pressure (up to 230 MPa) and pore pressure (up to 150 MPa) at both room and higher temperatures. Figure 5a shows the shear modulus at room temperature plotted as a function of confining pressure for various argon pore pressures. For the dry rock (i.e., without argon pore fluid), the shear modulus increases linearly with increasing confining pressure above 50 MPa, with a slope $\partial G/\partial P_c$ of about eight. The shear modulus decreases by as much as 6% when the rock is saturated with argon pore fluid at low pore pressures (1–7 MPa), but the dependence of the shear modulus upon confining pressure at low pore pressure is similar to that of the dry rock.

Further increasing the pore pressure at room temperature also lowers the shear modulus markedly. The reduction in the shear modulus is more pronounced at lower, rather than higher, confining pressure. For specimen #5, which was more extensively tested at room temperature, the variation of the shear modulus with confining pressure conforms very well to a linear relation, with a slope $(\partial G/\partial P_c)_{Pf}$, equal to approximately 40 for pore pressures of 50, 100, and 150 MPa.

Van der Molen (1979) determined the dependence of the shear modulus of Delegate aplite on confining pressure from ultrasonic (1-MHz) shear-wave velocity measurements on the dry rock at room temperature under confining pressures up to 300 MPa. His results are also shown in Figure 5a. Our results for the pressure dependence of the shear modulus are consistent with Van der Molen's (1979) ultrasonic data. However, there is a 3% difference in the values for the shear modulus obtained by the two experiments, presumably because of the different measuring systems and some variation between the rock specimens.

Figure 5b shows variations of the shear modulus with confining pressure and pore pressure under the more permeable conditions that prevail at higher temperatures (300°C and 600°C). There is no significant difference between moduli measured under dry conditions and those measured with argon saturation at low pore pressure (1 MPa). The shear modulus increases linearly with increasing confining pressure below a critical confining pressure (120 MPa at 300°C and 160 MPa at 600°C), with $\partial G/\partial P_c \sim 90$ at both temperatures for pore pressures ranging from 30 to 100 MPa. For similar pore pressures, this is more than twice the value at room temperature. Above the critical confining pressure, the shear modulus becomes much less sensitive to pressure.

Internal friction

Figure 6a shows representative data on the variation of internal friction with oscillation period. The significant scatter precludes definitive resolution of the frequency dependence. Therefore, the variation of Q^{-1} with temperature and argon pore pressure (Figure 6b) is best assessed from the average values for the entire 1–100-s range of the oscillation period. As in the dry rock, the internal friction of the argon-saturated rock increases with increasing temperature beyond about 400°C. For moderate confining pressures of 50–100 MPa, the internal friction measured at relatively high temperatures seems to increase with increasing pore pressure. However, Q^{-1} is lower for $P_f \sim 1$ MPa than for dry rock; as shown in Figure 6c, the effect is most pronounced at 50 MPa confining pressure. In contrast, for $(P_c, P_f) = (100, 50)$ MPa, Q^{-1} for the argon-saturated rock is significantly higher than for dry conditions (Figure 6b). No such variation of internal friction with pore pressure was detected at 150 MPa confining pressure.

Permeability measurements

In a previous set of measurements on Delegate aplite with an initial $p_0 = 0.1$ MPa, Lu and Jackson (1998) found that the rate constant A for pore-pressure equilibration remained low and almost temperature independent below a threshold T_c that increased systematically with increasing confining pressure from ~400°C at 50 MPa to ~550°C at 150 MPa. The rate constant A increased markedly with increasing temperature beyond T_c, indicating the development of enhanced crack connectivity (Lu and Jackson, 1998).

In the present study, we measured the transient flow resulting from a pore pressure increment δP_u or δP_d, which was superimposed upon an initial pore pressure p_0 greater than 25 MPa (Figure 4). Thus, as described above, we were able to determine the permeability k from the rate constant A. Figure 7a shows the values of the rate constant for pore-pressure equilibration A plotted against temperature for various pore pressures. Figure 7b shows the permeability k for only the higher pore-fluid pressures. On heating to 300°C, the permeability of the rock specimen remains almost unchanged [near

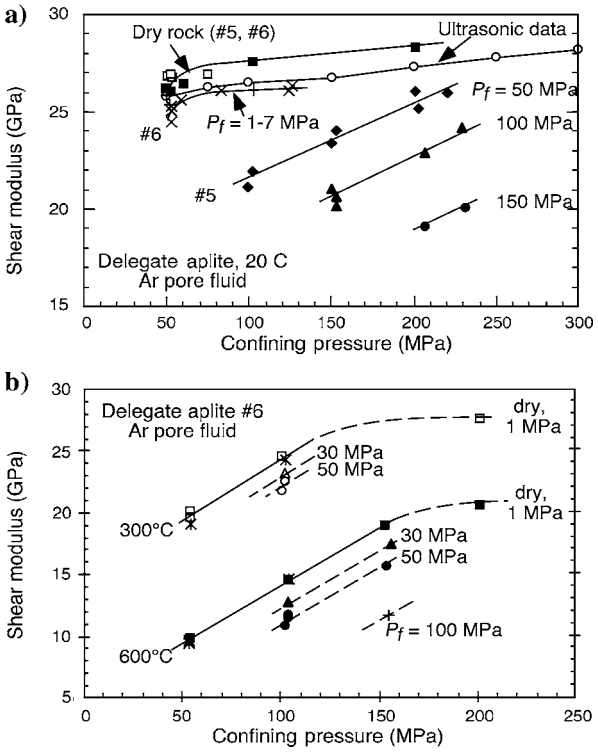

Figure 5. (a) Variation of the shear modulus with confining pressure P_c, in Delegate aplite (specimens #5 and #6) at room temperature under dry and argon-saturated conditions at different pore pressures, P_f. Specimen #5 was tested under the wider range of pressures (P_c, P_f). The ultrasonic data (open circles) were derived from the shear wave velocities of dry Delegate aplite measured by van der Molen (1979). (b) Variation of shear modulus with confining pressure in Delegate aplite at 300°C and 600°C and at various pore pressures. Open symbols: 300°C; solid symbols: 600°C.

10^{-19} m^2 or 10^{-7} darcy (D)], but it increases markedly when the temperature is increased further. Figure 8 shows the influence of confining pressure upon A and k. At relatively high temperature (e.g., 600°C), the measured permeability decreases with increasing confining pressure (that is, between 100 and 150 MPa) about twenty-fold for pore pressures of 28 and 50 MPa.

Crack porosity measurements

We measured the connected porosity of a thermally cycled specimen (#7) of Delegate aplite by the method described above (Experimental Procedure). We estimated the time required for pore pressure equilibration for any specific combination of temperature, confining and pore pressure from the permeability measurements described in the previous section. We found that the equilibration time varied from several minutes at temperatures above 400°C to several hours

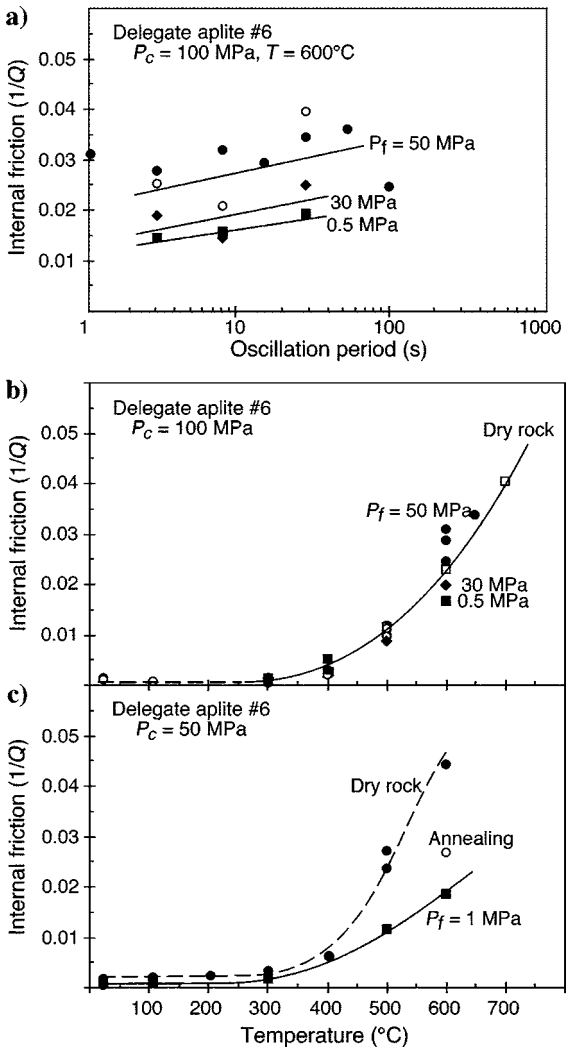

Figure 6. (a) Variation of internal friction with oscillation period for argon-saturated Delegate aplite at a confining pressure of 100 MPa and pore pressures of 0.5 MPa (squares), 30 MPa (diamonds), and 50 MPa (circles). (b) Variation of period-averaged internal friction for argon-saturated Delegate aplite with temperature and pore pressure at 100 MPa confining pressure. (c) Variation of the period-averaged internal friction with temperature for dry and argon-saturated Delegate aplite at 50 MPa confining pressure.

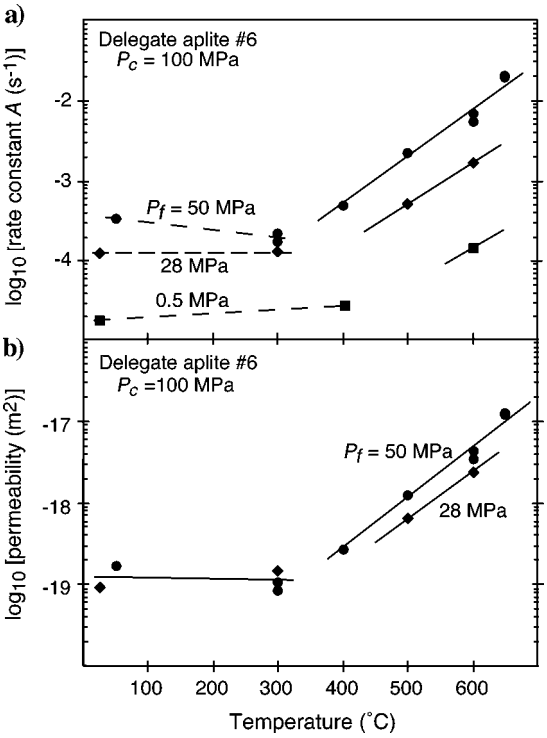

Figure 7. (a) Rate constant A for pore-pressure equilibration in Delegate aplite as a function of temperature, at confining pressure of 100 MPa and pore pressures of 0.5, 28, and 50 MPa. (b) The temperature dependence of permeability calculated for pore pressures $\geq$ 28 MPa from the values of A in (a).

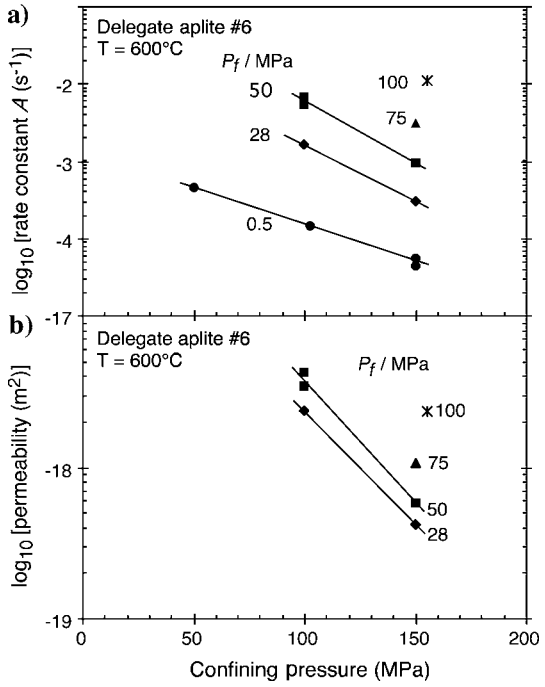

Figure 8. (a) The influence of confining pressure on the rate constant A for pore-pressure equilibration in Delegate aplite at 600°C and the indicated pore pressures. (b) Variation of permeability with confining pressure in Delegate aplite at 600°C for the indicated pore pressures as in (a).

at room temperature. Table 1 and Figure 9 show the results of these measurements under various conditions of temperature, confining pressure and pore pressure.

DISCUSSION

Influence of fluid saturation on elastic moduli and attenuation — Background

In a porous/cracked medium saturated with a relatively incompressible fluid, the application of an alternating stress causes essentially synchronous fluctuations in pore fluid pressure about the ambient value. Furthermore, this creates spatial gradients in pore pressure, both between the more- and less-compliant parts of the pore space (which have different orientations and/or aspect ratios) and between the interior of the laboratory specimen and the external pore-fluid reservoir. At sufficiently high frequencies ω as a result of its viscosity η, the fluid is able to support shear stress, with an effective modulus of $G = i\omega\eta$. It follows that, for all but the lowest frequencies, the effective moduli of a fluid-saturated medium should be higher than those for the corresponding dry medium for purely hydraulic reasons because the spatial scale for stress-induced fluid flow which is achievable during the period of the alternating stress is limited (e.g., O'Connell and Budiansky, 1977; their Figure 10).

Conceptually distinct relaxation phenomena are associated with transitions between different fluid-flow regimes: glued, saturated isolated, saturated isobaric, and drained (O'Connell and Budiansky, 1977; Endres and Knight, 1997; Pointer et al., 2000; Chapman et al., 2002). Figure 10 shows conditions for cracked media of low porosity and permeability. Accordingly, the well-known Biot relaxation in which modest levels of dispersion and attenuation are associated with the transition from a high-frequency regime ($> \omega_c = \eta\phi/\rho_f k$; Bourbié et al., 1987), in which inertial and viscous dissipative effects are significant to saturated isobaric conditions below ω_c, is not shown.

The effective elastic moduli of a cracked medium depend in principle upon both crack porosity ϕ and aspect ratio α (minimum/maximum dimension). However, for relatively low porosities and low aspect ratios (cracks), the behavior is controlled primarily by a single

Table 1. Results of connected porosity measurements on delegate aplite (specimen # 7) at given differential pressures and temperatures.

P_c (MPa)	P_f (MPa)	T (°C)	$(dx/dP_u)_R$ (mm/MPa)	$\sigma(dx/dP_u)_R$[a] (mm/MPa)	$(dx/dP_u)_0$ (mm/MPa)	$\Delta(dx/dP_u)$[b] (mm/MPa)	β_f[c] (MPa^{-1})	ρ_{RT} (g/cm^3)	ρ_T (g/cm^3)	ϕ_c	$\sigma(\phi_c)$
101	25	303	1.861	0.020	1.814	0.047	3.160E − 2	0.4131	0.1953	0.007	0.003
102	25.8	401	1.815	0.020	1.737	0.078	3.190E − 2	0.4131	0.1663	0.014	0.003
102	25.2	500	1.830	0.020	1.794	0.036	3.218E − 2	0.4131	0.1452	0.007	0.004
101	25	600	1.955	0.017	1.814	0.141	3.245E − 2	0.4131	0.1290	0.031	0.004
103	50.04	25	0.794	0.007	0.747	0.047	1.160E − 2	0.6928	0.6928	0.009	0.001
103	50.17	25	0.811	0.005	0.743	0.068	1.160E − 2	0.6928	0.6928	0.013	0.001
101	49.67	400	0.768	0.006	0.696	0.072	1.680E − 2	0.6928	0.3067	0.022	0.002
101	49.9	500	0.773	0.007	0.692	0.082	1.710E − 2	0.6928	0.2697	0.028	0.002
101	50.4	600	0.773	0.007	0.682	0.091	1.740E − 2	0.6928	0.2411	0.034	0.003
153	25.06	600	1.971	0.015	1.808	0.163	3.245E − 2	0.4131	0.1290	0.036	0.003
154	50.64	25	0.799	0.004	0.733	0.067	1.160E − 2	0.6928	0.6928	0.013	0.001
150	49.8	400	0.773	0.006	0.694	0.079	1.680E − 2	0.6928	0.3067	0.024	0.002
151	51.33	500	0.726	0.001	0.664	0.061	1.710E − 2	0.6928	0.2697	0.021	0.000
151	50.19	600	0.752	0.005	0.686	0.066	1.740E − 2	0.6928	0.2411	0.024	0.002
153	50.16	600	0.783	0.005	0.687	0.097	1.740E − 2	0.6928	0.2411	0.036	0.002
153	74.19	600	0.432	0.003	0.388	0.044	1.246E − 2	0.8556	0.3380	0.020	0.001
152	99.25	25	0.273	0.009	0.254	0.019	3.370E − 3	0.9644	0.9644	0.013	0.006
152	99.25	25	0.264	0.005	0.254	0.009	3.370E − 3	0.9644	0.9644	0.006	0.003
153	99.86	400	0.270	0.005	0.245	0.025	6.930E − 3	0.9644	0.5254	0.015	0.003
153	99.86	400	0.278	0.001	0.245	0.033	6.930E − 3	0.9644	0.5254	0.019	0.001
154	100.3	400	0.267	0.005	0.243	0.024	6.930E − 3	0.9644	0.5254	0.014	0.003
154	99.55	500	0.275	0.001	0.246	0.029	7.220E − 3	0.9644	0.4680	0.019	0.001
153	101.35	600	0.279	0.002	0.239	0.040	7.510E − 3	0.9644	0.4228	0.027	0.001
152	101.08	700	0.296	0.002	0.240	0.056	7.810E − 3	0.9644	0.3700	0.042	0.001
152	101.08	700	0.286	0.002	0.240	0.046	7.810E − 3	0.9644	0.3700	0.034	0.001

[a]The uncertainty $\sigma(dx/dP_u)_R$, inferred from scatter among redundant measurements, is used as a proxy for the uncertainty in the difference $\Delta(dx/dP_u)$.
[b]$\Delta(dx/dP_u) = (dx/dP_u)_R - (dx/dP_u)_0$.
[c]Fluid compressibility, $\beta_f = 1/K_f$.

variable known as crack density, ε (O'Connell and Budiansky, 1974). For a population of spheroidal inclusions of common aspect ratio, ε is given by

$$\varepsilon = 3\phi/4\pi\alpha. \tag{7}$$

This definition can be generalized to accommodate a distribution of crack aspect ratios. Figure 11 summarizes the sparse experimental observations concerning the effect of fluid saturation on the elastic moduli of cracked crystalline rocks with relatively low porosity. Together, ultrasonic, resonance, and forced-oscillation methods sample the mechanical relaxation spectrum of granite (Gordon, 1974) across eight decades of frequency. Figure 11 shows the fractional change in elastic wave speed that results from water saturation (with $P_f = 0$) plotted for the compressional (P), shear (S), and extensional bar (Y) modes.

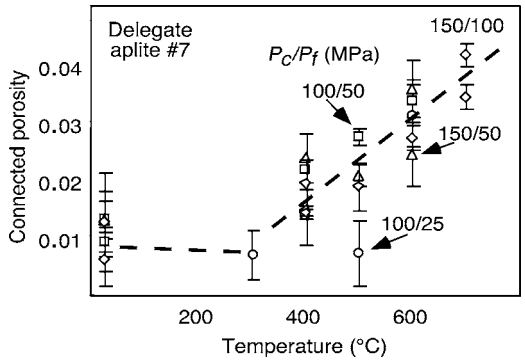

Figure 9. Temperature dependence of the connected porosity for different confining pressures and pore pressures.

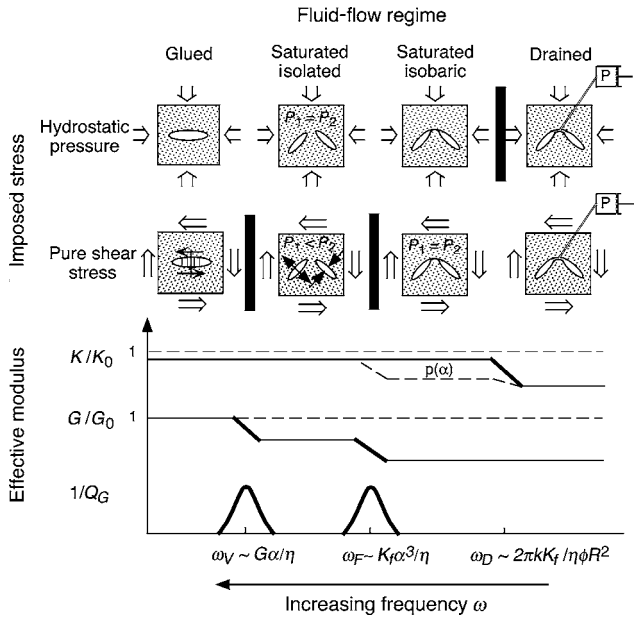

Figure 10. Fluid-flow regimes and effective elastic moduli for cracked and fluid-saturated rocks (O'Connell and Budiansky, 1977; redrawn after Jackson, 1991). The upper row of panels shows the response of the fluid-saturated medium to hydrostatic compression, whereas the lower row shows the response to shear. The vertical black bars highlight the transitions between fluid-flow regimes that are expected to cause marked modulus relaxation. P_1 and P_2 are the pore pressures in representative cracks of different orientation relative to the applied stress.

Figure 11 shows that, at ultrasonic frequencies (0.1–1 MHz), water saturation results in increased wave speeds with $\delta V_P/V_P \sim 0.2$ to 0.6 and $\delta V_S/V_S \sim 0$ to 0.1. Both V_P and V_S are typically higher than those calculated for saturated isobaric conditions. This suggests that the measurements sample the saturated isolated regime (as shown in Figure 10), in which grain-scale gradients in pore pressure are unrelaxed by local flow (O'Connell and Budiansky, 1977; Mavko and Jizba, 1991). For the kilohertz frequencies of resonant bar experiments, Gordon (1974) and Murphy (1984) reported higher wave speeds for water-saturated granites than for the corresponding dry rocks; the proportional effect of fluid saturation is apparently greater for the compressional and extensional modes than in shear. For partial saturation of Sierra white granite, Murphy (1984) measured slightly lower wave speeds than for the dry rock. Spencer (1981) found that $\delta V_Y/V_Y$ values obtained from extensional forced-oscillation experiments on Oklahoma granite changed sign from positive to negative with decreasing frequency between 400 and 4 Hz. Furthermore, Gordon (1974) found that, at frequencies of 100–10 mHz, the values of $\delta V/V$ are significantly negative for water saturation of Rhode Island granite.

Near-zero values of $\delta G/G$, and hence $\delta V_S/V_S$, are characteristic of the saturated isobaric regime, whereas near-zero values of $\delta K/K$ are indicative of the drained regime (Figure 10). Negative values of $\delta V/V$ in experimental data obtained at frequencies below 100 Hz cannot be explained by bulk fluid flow unless the crack density increases upon saturation (O'Connell and Budiansky, 1977). Alternatively, a reduction of wave speed upon saturation may reflect a reduction in the stiffness of grain contacts caused by adsorbed water (e.g., King, 1966; Tittmann et al., 1980; Spencer, 1981).

This interpretation of the broad trend evident in Figure 11 is reinforced by calculations of the relevant characteristic frequencies. For local fluid flow, $f_F = K_f\alpha^3/\eta \sim 10^3$ Hz for water saturation of cracks of aspect ratio $\alpha \sim 10^{-3}$. For the (radial) draining of a water-saturated cylindrical specimen of 1 cm diameter and permeability 10^{-18} m^2, $f_D = kK_f/\eta\phi R^2 \sim 1$ Hz.

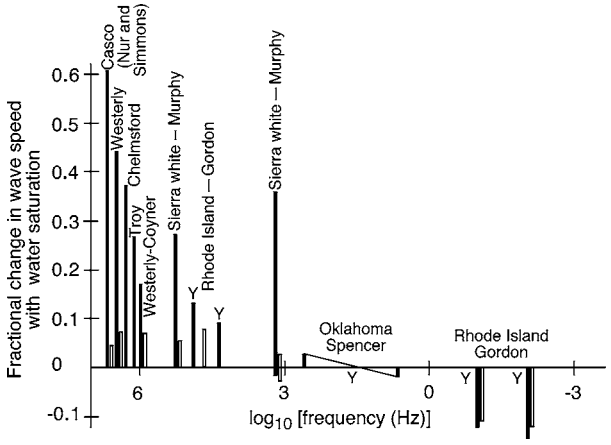

Figure 11. The effect of water saturation of granite at $P_c = P_f = 0$ on the speed of compressional (unlabelled solid bars), bar-mode longitudinal (solid bars labelled Y), and shear waves (unfilled bars). Data from Nur and Simmons (1969) for Casco, Chelmsford, Troy and Westerly granites; Gordon (1974) for Rhode Island granite; Spencer (1981) for Oklahoma granite; Murphy (1984) for Sierra white granite; and Coyner (1984) (cited in Mavko and Jizba, 1991) for Westerly granite.

For argon pore fluid at pressures from 10 to 100 MPa, K_f is substantially lower than for water at ambient conditions but, as shown in Figure 1, η is similarly lower. Thus, the quantity K_f/η and hence f_F, differs by less than an order of magnitude. In our experimental configuration, the cylindrical specimen was drained by longitudinal fluid flow to and from the external pore-pressure reservoirs, for which the rate is approximately the same as for pore-pressure equilibration (equation 6). The rate varies between 2×10^{-5} s^{-1} and 2×10^{-2} s^{-1} depending on the experimental conditions (Figures 7a and 8a). Therefore, we conclude that the low-frequency (<1 Hz) torsional-oscillation experiments of the present study probe the saturated isobaric and generally undrained regime — but shear mode properties are in any case unaffected by draining (Figure 10).

Crack porosity and crack connectivity

In the previous sections, we presented new experimental results concerning the shear mode seismic properties of Delegate aplite under conditions of varying confining pressure P_c argon pore pressure P_f and temperature. The difference between the measured modulus and that for the dry rock at room temperature and the same confining pressure, interpreted through the theory of O'Connell and Budiansky (1974), yields an estimate of the additional crack density ε resulting from thermal microcracking under the prevailing conditions of T, P_c, and P_f (Lu and Jackson, 1998). Because the measurements obtained in the present study sample the isobaric regime where the shear modulus is unaffected by the presence of the fluid (for given pore microstructure: Figure 10), the crack density can be estimated without encountering the ambiguities associated with fluid flow. However, somewhat higher values of crack density for a given modulus deficit δG would be expected from alternative models for $\delta G(\varepsilon)$, which differ significantly for $\varepsilon > 0.1$ (Sayers and Kachanov, 1991).

Lu and Jackson (1998) demonstrated that the rate constant A for the equilibration of pore pressure by fluid flow increases sharply at 350±50°C, 450±50°C and 550±50°C for confining pressures of 50, 100, and 150 MPa, respectively (Lu and Jackson, 1998, Figure 9). The shear-modulus deficits for each of these sets of conditions, interpreted in terms of crack density, yielded a critical value ε_{cr} = 0.16–0.18 for the percolation threshold (Lu and Jackson, 1998, Figure 13).

At the higher pore pressures of the present study, the permeability of the rock specimen has been rigorously calculated from the rate of growth or decay of $P_u(t)$ (equation 6). Figure 12a illustrates the covariation between permeability and inferred crack density for Delegate aplite for widely varying conditions of confining pressure (50–150 MPa), pore pressure (28–100 MPa), and temperature (25°–650°C).

The crack connectivity required for significant permeability is related to the probability p of crack intersection by percolation theory. For the four-coordinated Bethe network, the probability at the percolation threshold is $p_c = 1/3$, and the permeability beyond the percolation threshold is given by the relationship

$$k \propto (p - p_c)^{\nu}, \tag{8}$$

with $\nu = 2$ (Guéguen and Palciauskas, 1994). The probability p is related to crack density ε by

$$p = 1 - \exp(-\pi^2\varepsilon/4), \tag{9}$$

from which it follows that the percolation threshold $p = p_c$ corresponds to $\varepsilon = \varepsilon_c \sim 0.16$ (Le Ravalec and Guéguen, 1996). The crack density and permeability data of Figure 12a are entirely consistent with such predictions from percolation theory: with ε_c fixed at 0.16 and 0.17, respectively, comparably good least-squares fits to equations 8 and 9 yield $\nu = 2.3(4)$ and 2.0(4).

Figure 12b shows the measured connected porosity ϕ_c plotted against the crack density ε (as inferred from the modulus measurements) for the same confining pressures and pore pressures shown in Figure 12a. Although the data are scattered, it is evident that below the threshold crack density ε_c, ϕ_c increases only slightly as ε increases. Beyond ε_c, it increases more markedly with increasing ε, thus explaining the dramatic increase in permeability (Figure 12a).

Finally, with regard to the effect of confining or differential pressure on crack porosity, we note that the shear modulus approaches the value for zero pore pressure at sufficiently high P_{diff}, where the modulus presumably reflects the stiffness of the grain contacts (Figures 5b and 13b). Above a critical value of the differential pressure, P^*_{diff} (120 MPa at 300°C and 160 MPa at 600°C, as shown in Figure 13b), the slope, $\partial G/\partial P_{diff}$, has a low value ($\sim 8$). In contrast, it has a

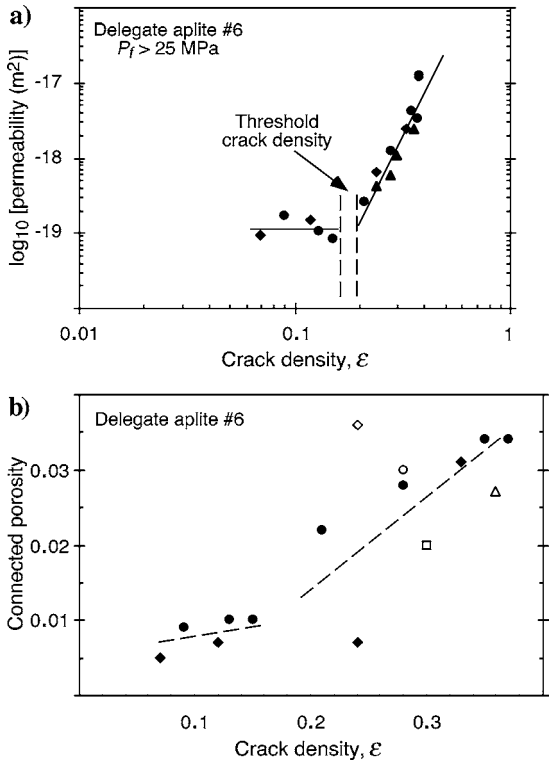

Figure 12. (a) The variation of permeability k in Delegate aplite with crack density ε as calculated from the shear modulus data with the model of O'Connell and Budiansky (1974). Data shown for the temperature range from 25°C to 650°C. Circles indicate P_c = 100 MPa and P_f = 50 MPa; diamonds indicate P_c = 100 MPa and P_f = 28 MPa; and triangles indicate P_c = 150 MPa and P_f = 25, 50, 75, 100 MPa. (b) The covariation of measured connected porosity against crack density, calculated from the shear modulus data for the following confining and pore pressures [P_c(MPa)/P_f(MPa)]: Diamonds — 100/28; solid circles — 100/50; open diamond — 150/28; open circle — 150/50; square — 150/75; and open triangle — 150/100.

much higher value (~90) below P^*_{diff}. The higher $\partial G/\partial P_{diff}$ below P^*_{diff} reflects the relative ease with which thermally induced cracks are closed by differential pressure. That such cracks are closed by differential pressures P^*_{diff} on the order of 100 MPa indicates that the aspect ratios $\alpha \sim P^*_{diff}/E$ (Walsh, 1965) are less than ~0.001 (where E is Young's modulus, ~100 GPa). Above P^*_{diff}, all of the thermal cracks close, and the lower $\partial G/\partial P_{diff}$ for this regime (still much larger than for the constituent minerals; e.g., $\partial G/\partial P_c = 0.46$ for quartz) reflects the closure of preexisting cracks with a wide range of higher aspect ratios.

The effective pressure

For porous/cracked rocks, many physical properties such as seismic velocity, porosity, or permeability are functions of both P_c and P_f. However, it is often possible and useful to define a quantity called the effective pressure, $P_{eff} = P_{eff}(P_c, P_f)$, such that P_{eff} applied alone as confining pressure would have the same effect on the property Y as the combination of P_c and P_f. That is,

$$Y(P_{eff}, 0) = Y(P_c, P_f) \tag{10}$$

(Bernabe, 1987; Guéguen and Palciauskas, 1994). The functional form of the effective pressure law depends on the physical property under consideration, as emphasized by Robin (1973). He also suggested that the concept of effective pressure may be most useful when it takes the special, simple form of the differential pressure (i.e., $P_{eff} = P_{diff} = P_c - P_f$), which can adequately describe many properties that are dependent upon the opening and closing of cracks. Robin (1973) assumed that all of the pores are fully interconnected and that the fluid pressure within them is at equilibrium, conditions which are not necessarily achieved during experimentation on tight crystalline rocks.

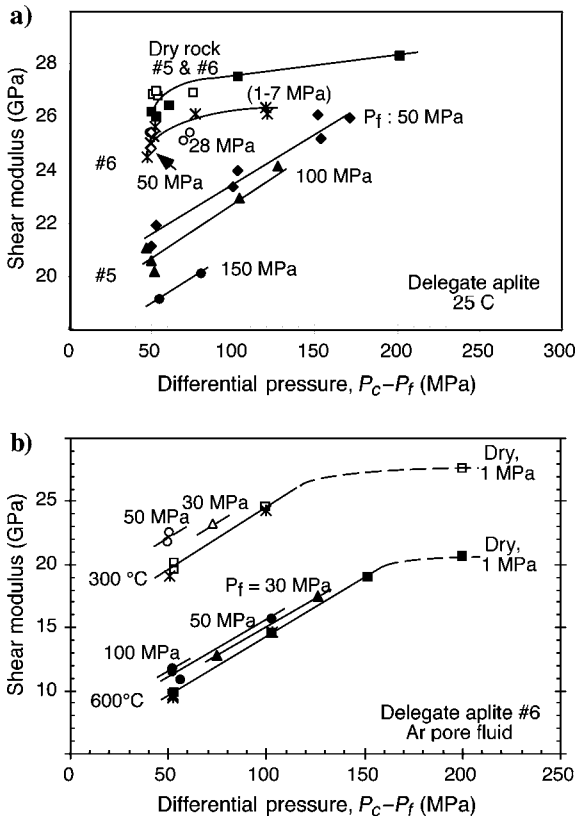

Figure 13. Variation of shear modulus with differential pressure, $P_{diff} = P_c - P_f$, for the Delegate aplite. (a) At room temperature. Open square — sample #6 (dry); solid square — sample #5 (dry). (b) At 300°C and at 600°C.

The following relation is a more general form for the effective pressure that is widely used:

$$P_{eff} = P_c - nP_f, \tag{11}$$

with n typically near one, and given by

$$n = -(\partial Y/\partial P_f)_{Pc}/(\partial Y/\partial P_c)_{Pf} \tag{12}$$

(e.g., Bernabe, 1987). Values of n greater than one indicate that Y has a greater absolute sensitivity to variation of the pore pressure than to variation of confining pressure. Values of n that are less than one indicate a lesser absolute sensitivity.

The low-frequency, forced-oscillation study presented here reveals systematic variations of the shear modulus with increasing P_c at constant P_f, and vice versa (Figure 5), which are redrawn with some additional data and with shear modulus plotted against differential pressure P_{diff} in Figure 13.

Room-temperature measurements

For the specimen #5 that was tested extensively at room temperature, the shear modulus is evidently much more sensitive to variations of P_f than to changes in P_c (Figure 5a). Saturation of this specimen with argon at low pore pressure (1–7 MPa) reduces the shear modulus by as much as 6%. At higher pore pressures, the measured modulus is also consistently very low, often lower than for dry conditions at 50 MPa confining pressure. This indicates the values of effective pressure were below 50 MPa (Figures 5a and 13a). In marked contrast, subsequent room-temperature measurements on sample #6 showed much smaller reductions in G for pore pressures of 28 and 50 MPa (Figure 13a). The different procedures used to generate the differential pressures in the two samples are thought to be responsible for these differences.

For sample #5, the desired pore pressure was established at a low effective pressure to take advantage of maximal permeability of the specimen. Progressively higher differential pressures (P_{diff}) were then achieved by increasing P_c at the prescribed value of P_f. However, as P_c increases, parts of the pore space with low aspect ratio will be closed, causing part of the previously interconnected pore space to become sealed off and thereby isolated. Pressures in these isolated cracks consequently increase when P_c is increased. Because the permeability of the rock at room temperature is very low, the overpressured pore fluid in the isolated cracks may persist within the specimen on the experimental time scale (a few hours). The isolated cracks presumably remain at higher values of pore pressure than the nominal value prescribed in the course of the experiments. Therefore, the actual pore pressure in part of the rock specimen may be substantially higher than the nominal value. As seen in Figure 7a, the range of the rate constants, from 2×10^{-5} to 3×10^{-4} s^{-1} for $T \leq 300$°C, gives direct evidence for the sluggishness of pore-pressure equilibration throughout the specimen (see Todd and Simmons, 1972).

At higher nominal pore pressure, more significant overpressure in the isolated cracks may result from the same P_c increase because the bulk modulus of pore fluid is higher. That may explain why G for a fixed P_{diff} decreases with increasing pore pressure (Figure 13a). Use

of the values of $\partial G/\partial P_f$ and $\partial G/\partial P_c$ inferred for specimen #5 at pore pressures of 50–150 MPa in equation 12 yields an apparent value of $n \sim 1.7$ for an effective pressure law, suggesting that the pore space is on average 70% overpressurized relative to the external reservoir.

Subsequently, for sample #6, we approached pore-pressure homogeneity more closely by monitoring the response of P_u to pressure changes imposed on the downstream reservoir under constant confining pressure (see Todd and Simmons, 1972). The much lower modulus measured on specimen #5 at nominal P_f = 50 MPa and P_c = 100 MPa (P_{diff} = 50 MPa) in comparision with sample #6, where the same pore pressure was generated at constant confining pressure of 100 MPa can be attributed to higher pore pressure in sample #5.

High-temperature measurements

Figure 13b shows the measurements of shear modulus for specimen #6 at high temperature plotted against differential pressure. The measurements were made after pore-pressure equilibration was achieved via the preferred procedure described under "Experimental Procedure." The values for the shear modulus at 1 MPa pore pressure are identical to those of the dry rock. This is consistent with the hypothesis that these measurements sample the saturated isobaric regime (Figure 10). At higher pore pressures, the confining and pore pressures have competing influences on the shear modulus of the argon-saturated granite, which are not adequately represented by the differential pressure P_{diff}. This requires that we instead use an effective pressure of the more general form, $P_{eff} = P_c - nP_f$, with the value of n calculated from equation 12. The values of n calculated for different pore pressures at 300° and 600°C are listed in Table 2. These values are consistently less than one, indicating greater sensitivity to confining pressure than pore pressure, but seem to approach unity more closely with increasing temperature.

The increase in G with increasing P_f for a given P_{diff} is less pronounced at the higher temperature. This phenomenon may reflect incomplete argon saturation of the crack porosity within the rock specimen. Because the permeability of the rock is still relatively low at 300°C (Figure 7b), not all cracks are accessible, and only a fraction of them are filled with argon pore fluid. As temperature increases, the permeability and crack density both increase and so does the proportion of accessible cracks, as suggested by the permeability and connected porosity measurements. Consequently, a smaller increase in the rigidity of the rock specimen is expected for a given increase in confining pressure at fixed pore pressure because the rock is more resistant to confining pressure as more cracks are filled with pore fluid. The value of n therefore increases toward one with the increasing inter-connectivity of the cracks resulting from increasing temperature.

Table 2. Estimation of the empirical factor n in the effective pressure laws describing the variations of shear modulus and permeability for Delegate aplite.

T (°C)	P_f (MPa)	$(\partial X/\partial P_f)_{P_c}$ [a]	$(\partial X/\partial P_c)_{Pf}$	n
$X = G$	—	—	—	—
300	28	—	—	0.61[b]
300	50	—	—	0.68[b]
600	28	−72.5 ± 1.8	89.4	0.81
600	50	−63.2 ± 1.1	76.4	0.83
600	100	—	—	0.83[b]
$X = \log k$	—	—	—	—
600	28-100	—	—	0.71[b]

[a] Average value for P_c values of 100 MPa and 150 MPa.
[b] Calculated from $(\partial X/\partial P_{diff})_{Pf} = (\partial X/\partial P_c)_{Pf}$, and $(\partial X/\partial P_f)_{P_{diff}} = (\partial X/\partial P_c)_{Pf} + (\partial X/\partial P_f)_{Pc}$, estimated from Figure 13 or 14.

Compressional and shear velocities measured at ultrasonic frequencies for fluid-saturated rocks are usually described adequately by an effective pressure law. The velocities are commonly somewhat less sensitive to variations of pore pressure than confining pressure (i.e., $n < 1$). Equivalently, velocities tend to increase slightly with increasing pore pressure P_f at fixed differential pressure, as seen in Figure 13b. Bourbié et al. (1987) attributed this effect to the increasing rigidity of the rock matrix with increasing confining pressure. Todd and Simmons (1972) established an effective pressure law with $n < 1$ for V_P in water-saturated Chelmsford granite. They found that n increases with increasing P_f, from 0.5 at 10 MPa through 0.75 at 30 MPa, to 0.85–0.90 for 50–105 MPa. Just as in our study, where n tends to increase with increasing temperature, the observations of Todd and Simmons might also be explained by changing crack connectivity. The more numerous measurements on porous sedimentary rocks (especially sandstones) also provide evidence of systematic departures from $n = 1$, which were interpreted by Christensen and Wang (1985) to reflect the differing responses of intergranular clay to changes in confining pressure and porewater pressure.

For the Delegate aplite used in this study, the permeability, like the shear modulus, is more sensitive to P_c than to P_f (Figure 14), which is consistent with an effective pressure law in which $n = 0.71$ (Table 2).

Attenuation mechanisms

In the discussion of fluid-flow regimes, we established that local fluid flow between adjacent thermally generated cracks of aspect ratio 0.001 should occur with a characteristic frequency $f_F \sim 10^3$ Hz and therefore that the experiments described here probe the saturated isobaric and undrained regimes (Figure 10). Accordingly, dissipation of the shear strain energy, which is associated with local fluid flow, would be expected to occur at much higher frequencies than those of the present study. Thus, other explanations must be sought for the observed dissipation.

Most of the data were obtained during heating to progressively higher temperatures. The lower levels of dissipation observed fol-

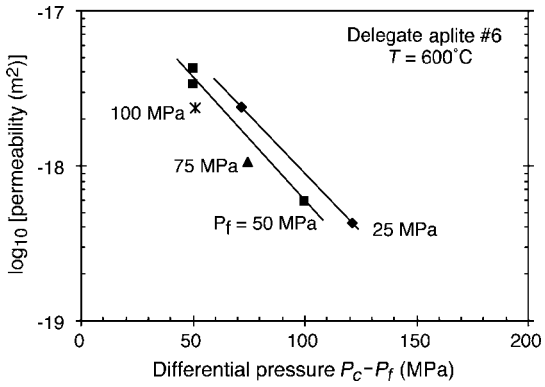

Figure 14. Variation of permeability with differential pressure for the indicated pore pressures for Delegate aplite at 600°C.

lowing high-temperature annealing (Figure 6c) are probably attributable to changed conditions at grain contacts, including the elimination of adsorbed moisture in the form of viscoelastic films. Similarly, and probably for the same reason, saturation with argon at low P_f results in systematically lower Q^{-1} especially under conditions of low confining pressure (Figure 6c). The dissipation decreases with increasing P_c (see Figure 6b and c). This is a well-known effect (e.g., Tittmann et al., 1980; Jackson et al., 1984) attributed to increased normal stress that inhibits the influence of adsorbed moisture at grain contacts. Finally, the trend of increasing dissipation with increasing pore pressure at constant P_c (Figure 6b) is presumably mostly attributable to decreasing differential pressure.

Significant strain-energy dissipation is observed only for temperatures above 300°C (Figure 6b), where mildly frequency-dependent absorption-band behavior is observed (Figure 6a). The Q^{-1} data are compatible, within the scatter of the data, with a power law dependence upon oscillation period with an exponent near 0.1 (see Jackson et al., 1992). Such high-temperature background is often attributed to the stress-induced migration of defects such as vacancies and other point defects and mobile dislocation segments, especially in regions of stress concentration near-grain contacts. Just as observed with the dry rock, Q^{-1} of the argon-saturated rock is frequency dependent at higher temperatures, although the data are somewhat scattered (Figure 6a).

CONCLUSIONS

The shear modulus and attenuation have been measured on a fine-grained granite (Delegate aplite) as functions of confining pressure ($P_c < 200$ MPa), argon pore-fluid pressure ($P_f < 150$ MPa), and temperature ($25 < T < 650$°C) at the low frequencies (10^{-2} – 1 Hz) of torsional forced-oscillation methods. These measurements are thought to probe the saturated isobaric regime, and to interpret them, we also conducted in-situ volumetric measurements of connected crack porosity and transient flow measurements of permeability.

The relationship between permeability and crack density that we inferred from the measured shear moduli using the model of O'Connell and Budiansky (1974) is consistent with the theoretical description of percolation behavior with a well-defined threshold at $\varepsilon_c \sim 0.17(2)$ and a power law exponent $\nu \sim 2$.

The low permeability $\sim 10^{-19}$ m^2 for $T < 300$°C means that pore-pressure equilibration occurs only over very long time scales. This complicates the room-temperature measurement of the effective pressure dependence of elastic properties. The shear modulus data obtained at 300 and 600°C can be reconciled with an effective pressure law in which $n < 1$ but increases toward unity with increasing crack connectivity. These findings are broadly consistent with those from ultrasonic measurements of compressional-wave speed in Chelmsford granite (Todd and Simmons, 1972).

The strain-energy dissipation becomes significant at temperatures above 300°C. It is dominantly high-temperature background dissipation and presumably results from the stress-induced migration of defects such as dislocations and grain boundaries. Q^{-1} is systematically reduced by annealing at high temperature, by the introduction of chemically inert argon pore fluid at low P_f, and by increasing P_c, which suggests that it results from viscoelastic effects at grain contacts.

Further clarification of the influence of fluid saturation on seismic wave speeds and attenuation in cracked media of low porosity will require the use of complementary ultrasonic, resonance, and forced-oscillation methods to probe the entire mechanical relaxation spectrum (Figure 11). Ideally, such experiments should be performed on a synthetic medium, analogous to sintered glass beads, but with low porosity and a narrow distribution of crack aspect ratios.

REFERENCES

Bernabe, Y., 1987, The effective pressure law for permeability during pore pressure and confining pressure cycling of several crystalline rocks: Journal of Geophysical Research, **92**, 649–659.

Biot, M. A., 1956a, Theory of propagation of elastic waves in a fluid-saturated porous solid, Part I, Low frequency range: Journal of the Acoustical Society of America, **28**, 168–178.

——–, 1956b, Theory of propagation of elastic waves in a fluid-saturated porous solid, Part II, Higher frequency range: Journal of the Acoustical Society of America, **28**, 179–191.

Bourbié, T., O. Coussy, and B. Zinszner, 1987, Acoustics of porous media, Gulf Publication Company.

Brace, W. F., J. B. Walsh, and W. T. Frangos, 1968, Permeability of granite under high pressure: Journal of Geophysical Research, **73**, 2225–2236.

Chapman, M., S. V. Zatsepin, and S. Crampin, 2002, Derivation of microstructural poroelastic model: Geophysical Journal International, **151**, 427–451.

Christensen, N. I., and H. F. Wang, 1985, The influence of pore pressure and confining pressure on dynamic elastic properties of Berea sandstone: Geophysics, **30**, 207–213.

Dvorkin, J., and A. Nur, 1993, Dynamic poroelasticity: A unified model with the squirt and the Biot mechanisms: Geophysics, **58**, 52–533.

Endres, A. L., and R. J. Knight, 1997, Incorporating pore geometry and fluid pressure communication into modelling the elastic behaviour of porous rocks: Geophysics, **62**, 106–117.

Gardner, G. H. F., 1962, Extensional waves in fluid-saturated porous cylinders: Journal of the Acoustical Society of America, **34**, 36–40.

Gassmann, F., 1951, Uber die Elastizitat porser Medien: Vierteljahrsschrift der Naturforschenden Gesellschaft Zürich, **96**, 1–23.

Gordon, R. B., 1974, Mechanical relaxation spectrum of crystalline rock containing water: Journal of Geophysical Research, **79**, 2129–2131.

Guéguen, Y., and V. Palciauskas, 1994, Introduction to the physics of rocks: Princeton University Press.

Hsieh, P. A., J. V. Tracy, C. E. Neuzil, J. D. Bredehoeft, and S. E. Silliman, 1981, A transient laboratory method for determining the hydraulic properties of "tight" rocks — Part I, Theory: International Journal of Rock Mechanics, Mining Sciences and Geomechanics Abstracts, **18**, 245–252.

Hudson, J. A., 1981, Wave speeds and attenuation of elastic waves in material containing cracks: Geophysical Journal of the Royal Astronomical Society, **64**, 133–150.

Jackson, I., 1991, The petrophysical basis for the interpretation of seismological models for the continental lithosphere: Geological Society of Australia Special Publication, **17**, 81–114.

Jackson, I., and M. S. Paterson, 1987, Shear modulus and internal friction of calcite rocks at seismic frequencies: Pressure, frequency and grain size dependence: Physics of the Earth and Planetary Interiors, **45**, 349–367.

——–, 1993, A high-pressure, high temperature apparatus for studies of seismic wave dispersion and attenuation: Pure and Applied Geophysics, **141**, 445–466.

Jackson, I., M. S. Paterson, and J. D. Fitz Gerald, 1992, Seismic wave dispersion and attenuation in Åheim dunite—An experimental study: Geophysical Journal International, **198**, 517–534.

Jackson, I., M. S. Paterson, H. Niesler, and R. M. Waterford, 1984, Rock anelasticity measurements at high pressure, low strain amplitude and seismic frequency: Geophysical Research Letters, **11**, 1235–1238.

Kachanov, M., 1993, Elastic solids with many cracks and related problems: Advanced Applied Mechanics, **30**, 259–445.

Kaye, G. W. C., and T. H. Laby, 1973, Tables of physical and chemical constants and some mathematical functions, 14th ed.: Longman Publishing Group.

King, M. S., 1966, Wave velocities in rocks as a function of changes in overburden pressure and pore fluid saturants: Geophysics, **31**, 50–73.

Le, Ravalec, M., and Y. Guéguen, 1996, High- and low-frequency elastic moduli for a saturated porous/cracked rock — Differential self-consistent and poroelastic theories: Geophysics, **61**, 1080–1094.

Lu, C., 1996, Shear mode anelasticity of thermally cracked and fluid-saturated rocks: Ph.D. thesis, Australian National University.

Lu, C., and I. Jackson, 1998, Seismic frequency laboratory measurements of shear mode viscoelasticity in crustal rocks, Part II, Thermally stressed quartzite and granite: Pure and Applied Geophysics, **153**, 441–473.

Mavko, G., and D. Jizba, 1991, Estimating grain-scale fluid effects on velocity dispersion in rocks: Geophysics, **56**, 1940–1949.

Mavko, G., and A. Nur, 1975, Melt squirt in the asthenosphere: Journal of Geophysical Research, **80**, 1444–1447.
Murphy, W. F., 1984, Seismic to ultrasonic velocity drift, intrinsic absorption and dispersion in crystalline rock: Geophysical Research Letters, **11**, 1239–1242.
———, 1985, Sonic and ultrasonic velocities: theory versus experiment: Geophysical Research Letters, **12**, 85–88.
Murphy, W. F., K. W. Winkler, and R. L. Kleinberg, 1984, Frame modulus weakening in sandstones, The effect of adsorption on surface energy: Geophysical Research Letters, **11**, 805–808.
Neuzil, C. E., C. Cooley, S. E. Silliman, J. D. Bredehoeft, and P. A. Hsieh, 1981, A transient laboratory method for determining the hydraulic properties of 'tight' rocks, Part II, Application: International Journal of Rock Mechanics Mining Sciences and Geomechanics Abstracts, **18**, 253–258.
Nur, A., and G. Simmons, 1969, The effect of saturation on velocity in low porosity rocks: Earth and Planetary Science Letters, **7**, 183–193.
O'Connell, R. J., and B. Budiansky, 1974, Seismic velocities in dry and saturated cracked solids: Journal of Geophysical Research, **79**, 5412–5426.
———, 1977, Viscoelastic properties of fluid-saturated cracked solids: Journal of Geophysical Research, **82**, 5719–5735.
Paffenholz, J., and H. Burkhardt, 1989, Absorption and modulus measurements in the seismic frequency and strain range on partially saturated sedimentary rocks: Journal of Geophysical Research, **94**, 9493–9507.
Pointer, T., E. Liu, and J. A. Hudson, 2000, Seismic wave propagation in cracked porous media: Geophysical Journal International, **142**, 199–231.
Robin, P. F., 1973, Note on effective pressure: Journal of Geophysical Research, **78**, 2434–2437.
Sayers, C. M., and M. Kachanov, 1991, A simple technique for finding effective elastic constants of cracked solids for arbitrary crack orientation statistics: International Journal of Solids Structures, **27**, 671–680.
Schubnel, A., and Y. Guéguen, 2003, Dispersion and anisotropy of elastic waves in cracked rocks: Journal of Geophysical Research, **108**, 2101–2116, doi: 10.1029/2002JB001824.
Spencer, J. W., 1981, Stress relaxations at low frequencies in fluid-saturated rocks, Attenuation and modulus dispersion: Journal of Geophysical Research, **86**, 1803–1812.
Stewart, R. B., and R. T. Jacobson, 1989, Thermodynamic properties of argon from the triple point to 1200 K with pressures to 1000 MPa: Journal of Physical and Chemical Reference Data, **18**, 639–798.
Tittmann, B. R., J. R. Bulau, and M. Abdel-Gawad, 1984, Dissipation of elastic waves in fluid saturated rocks: Conference Proceedings, American Institute of Physics, 107, 131–143.
Tittmann, B. R., V. A. Clark, J. M. Richardson, and T. W. Spencer, 1980, Possible mechanisms for seismic attenuation in rocks containing small amounts of volatiles: Journal of Geophysical Research, **85**, 5199–5208.
Todd, T., and G. Simmons, 1972, Effect of pore pressure on the velocity of compressional waves in low-porosity rocks: Journal of Geophysical Research, **77**, 3731–3743.
van der Molen, I., 1979, Some physical properties of granite at high pressure and temperature: Ph.D. thesis, Australian National University.
Vidal, D., R. Tufeu, Y. Garrabos, and B. Le Neindre, 1979, Thermophysical properties of noble gases at room temperature up to 1 GPa, *in* B. Vodar and P. Marteau, eds.: High pressure science and technologies: Pergamon Press.
Walsh, J. B., 1965, The effect of cracks on the compressibility of rock: Journal of Geophysical Research, **70**, 381–389.
———, 1969, New analysis of attenuation in partially melted rock: Journal of Geophysical Research, **74**, 4333–4337.
Winkler, K. W., 1985, Dispersion analysis of velocities and attenuation in Berea sandstone: Journal of Geophysical Research, **90**, 6793–6800.
———, 1986, Estimates of velocity dispersion between seismic and ultrasonic frequencies: Geophysics, **51**, 183–189.
Zhang, S., M. S. Paterson, and S. F. Cox, 1994, Porosity and permeability evolution during hot isostatic pressing of calcite aggregates: Journal of Geophysical Research, **99**, 15741–15760.